Probing interdendritic flow and hot tearing during solidification using real time X-ray imaging and droplet tracking

E. Liotti*[1], A. Lui[1], T. Connolley[2], and P.S. Grant[1]

[1]Department of Materials, University of Oxford, Parks Road, Oxford OX1 3PH, UK

[2]Diamond Light Source, Harwell Science and Innovation Campus, Didcot, OX11 0DE, UK.

Abstract

Despite the well-known importance of controlling shrinkage-induced liquid flow in alloy castings to avoid the formation of catastrophic hot tears during the final stages of solidification, there has been little direct experimental measurement of liquid metal flow and hot tear formation under practical conditions. We use synchrotron X-rays to obtain radiographic video sequences of the solidification of monotectic Al-Pb alloys in which Pb droplets form as a fine-scale emulsion. We track and measure the velocity of thousands of Pb droplets as they move through interdendritic regions due to the effect of liquid to solid shrinkage during the final stages of solidification, up to the point of hot tear formation. Based on the droplet velocities, we present an analysis to estimate the interdendritic liquid velocity as solid fraction increases, and thus the shrinkage pressure drop driving the flow. The analysis is applied for video sequences obtained for both equiaxed and columnar microstructures, each under a range of cooling rates. Our measurements of the critical shrinkage-induced pressure for hot tear formation agree well with

prior model-based and theoretical suggestions. The limitations and prospects for droplet tracking measurements of liquid metal flows are discussed.

1 Introduction

Avoiding defect formation during the solidification of high value shaped and continuous cast products is a critical technological objective, and continues to attract significant research attention [1–4]. Defects that arise during casting include gas-induced porosity, residual stresses and arising distortion, elemental macro-segregation and hot tearing. Hot tearing is a highly undesirable, large-scale and damaging planar discontinuity in the cast microstructure related to the inhibited movement of liquid, particularly in the stages of solidification when the alloy is in the mushy, solid-liquid state. In this mushy state, the principle reason for liquid movement is to "feed" the volume change (shrinkage) associated with the liquid-to-solid phase transition of most engineering alloys based on Fe, Al, Ni or Ti, which typically lies in the range 3 to 5% [1, 5–9]. The internal, pressure drop associated with the progressive formation of solid draws residual liquid through and deeper into the largely solid dendrite network. Where this flow becomes restricted e.g. at high solid fraction as the dendrite network becomes increasingly impermeable, large shrinkage pores (often arising from smaller gas pores) can develop, progressing into larger-scale planar tears of at least millimetre-scale, especially at tensile stress raising features such as corners in shaped castings [1, 2]. In unfed regions of the casting, the resulting negative hydrostatic pressures may become so large that macroscopic, large-scale movement or collapse of the dendrite network occurs, causing further tearing of the microstructure and induced flow of solute-rich or solute-denuded liquid over large distances to form damaging inter-dendritic "segregates" in the final structure [1, 2]. For shaped castings, there is usually no opportunity to remove these tears and defects by mechanical processing, and even in wrought products, the damaging effect of severe porosity and macro-segregation cannot be ameliorated by subsequent thermo-mechanical processing such as rolling, forging or heat treatments.

The feeding of shrinkage and avoidance of tearing in castings has been achieved through careful design of the casting geometry (such as the position, size and number

of feeders and risers), the development of alloys with intrinsically low overall shrinkage (e.g. cast irons), alloys with narrow freezing ranges (e.g. near eutectic Al-Si), alloys with high intrinsic fluidity, and the addition of grain refiners (e.g. TiB_2 in Al alloys) to promote equiaxed over dendritic microstructures because equiaxed grains are better able to move and accommodate liquid flow [1]. There has also been extensive modelling of alloy solidification that includes shrinkage and resulting liquid flow effects of ever-increasing sophistication, which can be used to guide casting design and conditions [10–19]. However, there have been very few reports of experiments that measure directly or infer the forces and pressures that lead to liquid flow and hot tearing in castings under realistic conditions [20].

In this paper we use synchrotron X-rays to obtain radiographic video sequences of the solidification of a monotectic Al-Pb alloy in which Pb droplets form as a fine-scale emulsion in the liquid during solidification of the dendritic, primary Al-phase. By tracking the movement of thousands of Pb droplets through the inter-dendritic regions and applying a simple analysis, we calculate the liquid velocity and the associated pressure drop. We show significant differences between equiaxed and columnar microstructures. Calculations of shrinkage-induced pressure drop agree well with previous modelling and theory-based estimates, and the onset of hot tearing. Finally, we discuss the limitations and potential for the novel droplet tracer tracking approach.

2 Experimental method

In situ synchrotron X-ray radiography studies of the solidification of Al-1wt%Pb were carried out at the B16 beamline at the Diamond Light Source, UK. The beamline was used in monochromatic mode, tuning the beam to an energy of $18\,\mathrm{keV}$ with a high flux double multilayer monochromator (Ru/B_4C). The transmitted signal was collected on a $500\,\mu\mathrm{m}$ thick $CdWO_4$ scintillator combined with a PCO.Edge detector attached to an optical module to give a spatial resolution of $1.65\,\mu\mathrm{m/pixel}$ with a field of view (FOV) of $\sim 3.5\,\mathrm{mm} \times 4.2\,\mathrm{mm}$ at frame rates between $6\,\mathrm{fps}$ to $8.5\,\mathrm{fps}$. The experiments were conducted using a bespoke solidification rig comprising a miniature Bridgman furnace, a comprehensive description of which can be found in [21]. Thin foil samples ($\sim 200\,\mu\mathrm{m}$)

of slightly hypo-eutectic composition (Al-1wt%Pb), with and without grain refiners (0.2 wt% Ti using a Al-5Ti-1B master alloy), were prepared from high purity Al and Pb following the same procedure described in [22, 23]. During the experiments, samples were heated above the liquidus temperature and held for a few minutes to melt the solid phase and ensure all Pb was in solution in the liquid. Then, the temperature of the heaters was decreased at a constant and controlled cooling rate, maintaining near isothermal conditions, while recording radiographic videos. In total 5 video sequences were recorded: three of a non grain refined sample, which solidified with a columnar microstructure, cooled at $0.2\,\mathrm{K\,s^{-1}}$, $0.7\,\mathrm{K\,s^{-1}}$ and $2\,\mathrm{K\,s^{-1}}$; and two of a grain refined sample with equiaxed microstructure, cooled at $0.7\,\mathrm{K\,s^{-1}}$ and $2\,\mathrm{K\,s^{-1}}$. Fig. 1 is the equilibrium Al-Pb phase diagram showing the solidification path of Al-1wt%Pb cooled from the liquid (yellow line). On reaching the liquidus, crystals of almost pure Al nucleate and grow in the liquid, releasing latent heat and slowing the cooling rate until a solid fraction of approximately 0.28 at the monotectic temperature of $932\,\mathrm{K}$. At this point the invariant reaction $L_1 \rightarrow L_2 + Al_{(solid)}$ occurs (where L_1 is 1.4wt%Pb and L_2 is 99.82wt%Pb), the existing Al grains continue to grow (all nucleation has already taken place) and L_2 droplets begin to nucleate in the L_1 liquid interdendritic channels. The temperature remains approximately constant until the solid fraction reaches 0.99, then cooling resumes and solidification ends at $600.15\,\mathrm{K}$ when the Pb droplets solidify fully. As shown later, the alloy thus comprises principally of α-Al, with a fine dispersion of Pb in the interdendritic regions.

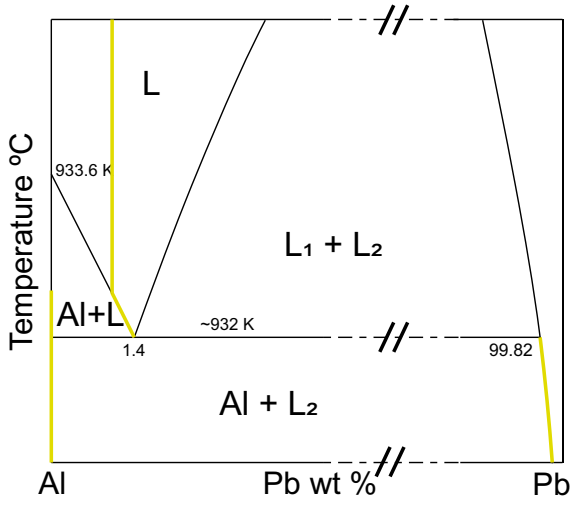

Figure 1: The equilibrium Al-Pb phase diagram adapted from [24].

3 Analysis

3.1 Pb droplet tracking

Raw images from the solidification video sequences were firstly pre-processed to correct for background inhomogeneity and noise (flat field correction followed by a Gaussian filter with 3×3 pixels window size and $\sigma = 2$), and the subsequent analysis was automated using a bespoke Matlab algorithm. Individual Pb droplets in each frame were detected by segmenting the difference image obtained by subtracting the previous frame from the current frame, and Pb droplets diameter and location information stored frame-to-frame. By recognizing the same droplet in adjacent frames and knowing the time between frame, a velocity vector could be assigned to each droplet, a technique widely-known as particle image velocimetry (PIV) [25]. For each frame pair, the identification of droplets was achieved using the Matlab built-in version of the Farneback optical flow algorithm [26] to estimate droplet motion and a "k-nearest neighbours approach" to match stored droplet coordinates with the newly discovered droplets in the current frame. Non-assigned droplet pairs were discarded for that frame, but then re-assessed for pairing in the next image pair. Typically, frame-to-frame tracking allowed the velocity, acceleration and diameter of a few thousands droplets in each video sequences to be obtained. The algorithm was validated against manual measurements by eye, and details of the procedure are reported in section S.1 of the Supplementary Information.

3.2 Interdendritic channel width

The width of interdendritic channels was estimated using a bespoke image analysis procedure comprising the following processing steps (shown in Fig. 2):

1. A map of the interdendritic channels was produced thresholding the image obtained by summing up all L_2 droplet traces in each frame, which were generated by binarizing the frames to segment the droplets.

2. The Euclidean distance transform of the inverted interdendritic channel map was computed; each pixel in the new map was assigned the value of the distance

between that pixel and the closest edge of the interdendritic channel (distance values in μm).

3. Channel widths were extracted by skeletonizing the Euclidean distance transform map, which returned the value of the channel centerline pixels equivalent to the channel half-width at the given location.

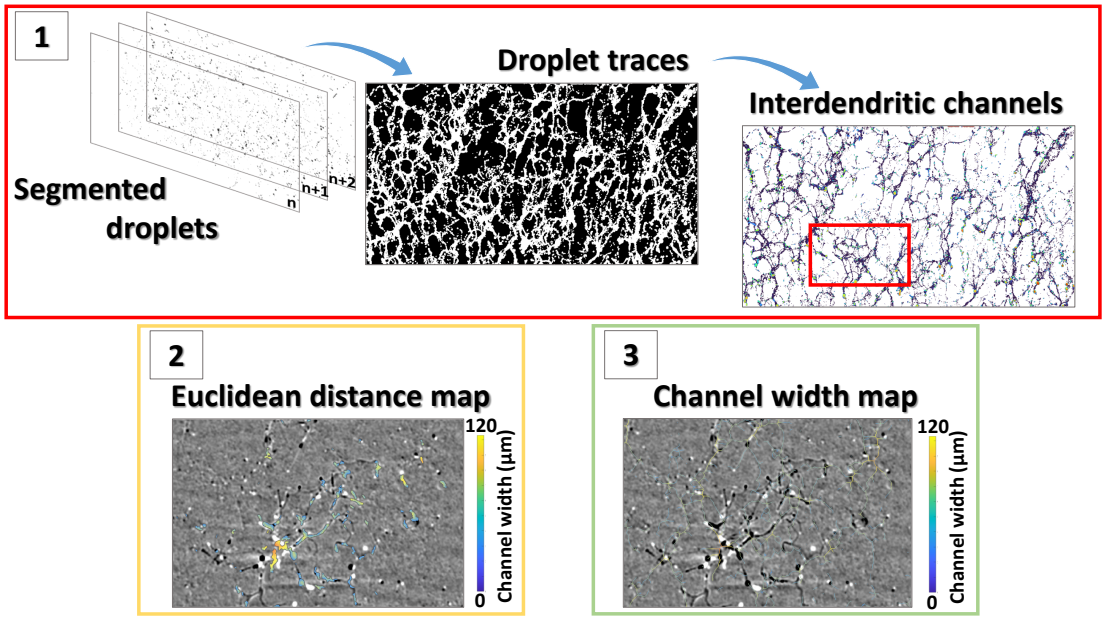

Figure 2: Image processing steps to estimate interdendritic channel widths. Steps 2 and 3 show the region of interest highlighted in red in step 1.

3.3 Liquid flow and pressure drop

The flow of L_1 liquid in the mushy zone was estimated by tracking the motion of thousands of droplets (L_2 liquid) forming within the interdendritic channels, from which the L_1 liquid velocity was calculated as follows. The motion of the spherical Pb droplets with radius r is described by a force balance [27–36]:

$$\rho_2 r^3 \frac{d\boldsymbol{u_2}}{dt} = F_g(r) + F_S(r) + F_M(r, T, c) \tag{1}$$

where ρ_2 is the density of the Pb-rich droplet, $\boldsymbol{u_2}$ is the droplet velocity vector, F_g is the gravity force, F_S is the Stokes friction force, F_M is the thermosolutal-capillary

Marangoni force, T is the temperature and c is the solute concentration of the L_1 liquid. Expanding the right-hand side of Eq. 1 gives:

$$F_g(r) + F_S(r) + F_M(r,T,c) = \Delta\rho r^3 \boldsymbol{g} + 6\eta_1 \frac{2\eta_1 + 3\eta_2}{\eta_1 + \eta_2} r\Delta\boldsymbol{u} + r^2 \frac{3\eta_1}{\eta_1 + \eta_2}\left[\frac{\kappa_1}{2\kappa_1 + \kappa_2}\frac{\partial\sigma}{\partial T}\nabla T + \frac{D_1}{2D_1 + D_2}\frac{\partial\sigma}{\partial c}\nabla c\right] \quad (2)$$

where $\Delta\rho = \rho_2 - \rho_1$ is the L_2 - L_1 liquid density difference, $\boldsymbol{g}$ is the gravitational acceleration vector, η_i is the dynamic viscosity of the L_i liquid, $\Delta\boldsymbol{u} = \boldsymbol{u_1} - \boldsymbol{u_2}$ is the velocity difference between the Pb droplets and the surrounding liquid, κ_i is the L_i thermal conductivity, σ is the Al-Pb interfacial tension, and D_i is the L_i mass diffusion coefficient. The index $i = 1, 2$ refers to the Al-rich liquid (1.4 wt%Pb) and the liquid in the droplet (99.82 wt%Pb) respectively.

Inspection of Eq. 2 shows that the gravity force has a cubic dependency with droplet radius, whereas the drag force depends linearly on droplet radius and velocity difference. The Marangoni force varies as the square of radius and with temperature and composition gradients in the L_1 liquid that cause a gradient in interfacial tension at the droplet-liquid interface.

The requirement for the analysis is to obtain the interdendritic liquid velocity $\boldsymbol{u_1}$ as a function of the spatially and temporally resolved measurements of droplet radius r, velocity $\boldsymbol{u_2}$ and acceleration $\frac{d\boldsymbol{u_2}}{dt}$. However, solving Eq. 2 is hampered by the unavailability or uncertainty of the Marangoni force-related terms $\frac{\partial\sigma}{\partial T}\nabla T$ and $\frac{\partial\sigma}{\partial c}\nabla c$.

As a first step to simplify Eq. 2 it is typically assumed that for monotectic alloys (such as Al-Pb used here) and according to the equilibrium phase diagram, the solute term $\nabla c \approx 0$ [32–34, 36]. This approximation is supported by the radiographic sequences that show no resolvable Pb gradient in the liquid. As a result Eq. 2 becomes:

$$F_g(r) + F_S(r) + F_M(r,T,c) = \Delta\rho r^3 \boldsymbol{g} + 6\eta_1 \frac{2\eta_1 + 3\eta_2}{\eta_1 + \eta_2} r\Delta\boldsymbol{u} + r^2 \frac{3\eta_1}{\eta_1 + \eta_2}\left[\frac{\kappa_1}{2\kappa_1 + \kappa_2}\frac{\partial\sigma}{\partial T}\nabla T\right] \quad (3)$$

Parameter	Value	Ref.
ρ_{Al}	$2375\,\mathrm{kgm}^{-3}$	[32]
ρ_{Pb}	$10\,678\,\mathrm{kgm}^{-3}$	[37]
η_{Al}	$1.38\times10^{-3}\,\mathrm{kg\,(m\,s)}^{-1}$	[38]
η_{Pb}	$1.41\times10^{-3}\,\mathrm{kg\,(m\,s)}^{-1}$	[38]
κ_{Al}	$91\,\mathrm{W\,(m\,K)}^{-1}$	[38]
κ_{Pb}	$15\,\mathrm{W\,(m\,K)}^{-1}$	[38]
$\frac{\partial\sigma}{\partial T}$	$-1.0976\times10^{-4}\,\mathrm{J\,m^{-2}\,K^{-1}}$	[30]

Table 1: The thermophysical properties used in Eq. 3.

Next, to further simplify Eq. 3 we consider the likely relative magnitude of the three remaining terms on the right hand side of Eq. 3 under experimental conditions and using the thermophysical properties provided from the literature, given in Tab. 1. The temperature dependency of the interfacial tension $\frac{\partial\sigma}{\partial T}$ in Tab. 1 was estimated from [30, 36]:

$$\sigma = \sigma_0(1-\frac{T}{T_0})^{1.26} \tag{4}$$

where $\sigma_0 = 0.328\ \mathrm{J\,m^{-2}}$ at temperature T_0, which gives

$$\frac{\partial\sigma}{\partial T} = -1.26\sigma_0\frac{1}{T_c}(1-\frac{T}{T_c}) \tag{5}$$

where the monotectic temperature $T = 932\,\mathrm{K}$ and $T_c = 1695.4\,\mathrm{K}$ [30, 36]. The temperature gradient ∇T was measured by tracking the tip of the columnar dendrites in video2 as $2\,\mathrm{K\,mm^{-1}}$.

Fig. 3 shows the range of droplet radius measured from the radiographs, with a number mean of $\approx 5\,\mu\mathrm{m}$ and an upper bound of $\approx 10\,\mu\mathrm{m}$. The corresponding droplet velocity distributions are presented in more detail later, but were typically $100\,\mu\mathrm{m\,s^{-1}}$, ranging up to $200\,\mu\mathrm{m\,s^{-1}}$. Using these data, Fig. 4 shows the magnitude of gravity, Stokes and Marangoni forces acting on droplets. The Stokes force was estimated for three differential velocities of $\Delta\boldsymbol{u} = 50\,\mu\mathrm{m\,s^{-1}}$, $100\,\mu\mathrm{m\,s^{-1}}$ and $200\,\mu\mathrm{m\,s^{-1}}$. For a $3\,\mu\mathrm{m}$ radius droplet, the Stokes force was in the range $3.1\,\mathrm{pN}$ to $12.5\,\mathrm{pN}$, the gravity force was $2.2\,\mathrm{pN}$ and the Marangoni force was $1.3\,\mathrm{pN}$. For a $6\,\mu\mathrm{m}$ droplet radius, the same forces were $6.2\,\mathrm{pN}$ to $25\,\mathrm{pN}$, $18\,\mathrm{pN}$ and $5.4\,\mathrm{pN}$.

For the most prevalent droplet sizes and velocities, the simplified Marangoni force

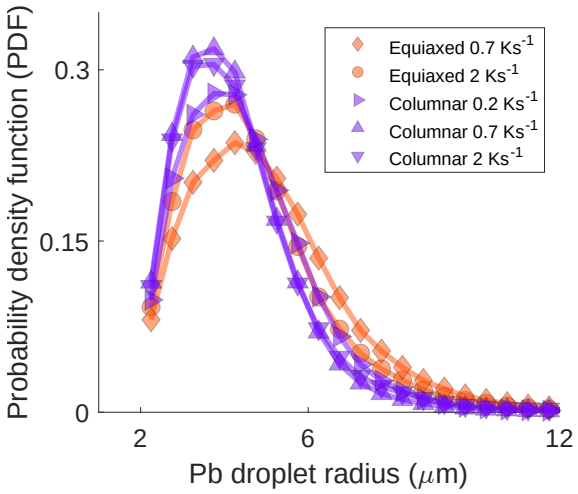

Figure 3: Pb droplet radius distribution.

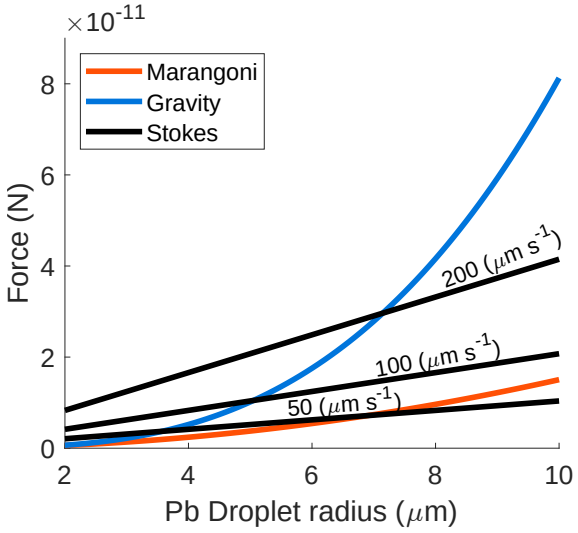

Figure 4: Forces estimation as a function of the Pb droplet radius.

was approximately no more, and usually significantly less, than 50% of either the Stokes or gravity force. Therefore, for simplicity the third term on the right hand side of Eq. 3 was also assumed to be zero. As the analysis showed, there will be a Marangoni force contribution to droplet motion, but under the conditions of the current work, it was relatively small.

Thus simplifying, rearranging and combining with Eq. 1 to obtain the liquid velocity $\boldsymbol{u_1}$ in terms of known parameters and experimental data yields:

$$\boldsymbol{u}_1 = \boldsymbol{u}_2 + \frac{r^2(\rho_2 \frac{d\boldsymbol{u_2}}{dt} - \Delta\rho\boldsymbol{g})}{6\eta_1 \frac{2\eta_1+3\eta_2}{\eta_1+\eta_2}} \tag{6}$$

Then, having obtained the liquid velocity $\boldsymbol{u}_1$, the pressure drop that drives this flow ΔP in L_1 was estimated using the well-known Darcy equation:

$$\Delta P = -\frac{u_1 \eta_1}{K} \tag{7}$$

where K is the permeability of the mushy zone. The mushy zone permeability K was calculated for each frame of the radiographic sequences (i.e. for each time step) and assumed constant across the field of view (FOV) at that instant. For columnar microstructures the flow was mainly parallel to the primary dendrite arms, and the Blake-Kozeny relationship [39] was used:

$$K = C\lambda^2 \frac{f_l^3}{(1-f_l)^2} \tag{8}$$

where $C = 8.5 \times 10^{-4}$ is a fitting constant [40], $\lambda = 1.3\,\mathrm{mm}$ is the average primary arm spacing from the radiographs and f_l is the liquid fraction.

For the equiaxed microstructures, a Kozeny-Carman relationship [41] was used:

$$K = \frac{\lambda^2}{180} \frac{f_l^3}{(1-f_l)^2} \tag{9}$$

where $\lambda = 0.221\,\mathrm{mm}$ is the average secondary arm spacing from the radiographs. The evolution of solid fraction f_s = 1 - f_l was obtained by setting $f_s = 0$ in the first frame in which a solid crystal was first observed and $f_s = 1$ in the frame immediately after any hot tearing was observed. Note that because solidification took place at an invariant temperature, more typical approaches to estimate solid fraction evolution as a function of temperature, such as the level rule or Scheil equation, could not be used.

4 Results

Fig. 5 shows two image sequences of the flow of Pb droplets within the interdendritic channels of mushy zones for two different α-Al morphologies, from the appearance of the first droplets to the final formation of hot tears. Readers are invited to watch the video sequences on-line (video1 and video2). Figs. 5(a, c, e, g and i) are from grain

refined Al-1wt%Pb cooled at $0.7\,\mathrm{K\,s^{-1}}$ that consisted of equiaxed α-Al grains with an average size of $\sim 200\,\mu\mathrm{m}$. Figs. 5(b, d, f, h and j) are a solidification sequence of non-grain refined Al-1wt%Pb cooled at $2\,\mathrm{K\,s^{-1}}$ where only three, millimeter-scale columnar dendrites grew within the FOV.

In both experiments average droplet velocities sharply increased to a peak over a few seconds and then decreased to almost zero as the solid fraction increased to above 0.7. The average droplet radius steadily increased, primarily due to hydrodynamically driven coalescence [27, 28], from an initial average of $3.5\,\mu\mathrm{m}$ to $\sim 6\,\mu\mathrm{m}$. Only moving droplets were detected, and any droplet with a radius smaller than $2\,\mu\mathrm{m}$ was filtered out as it was below the spatial resolution limit and thus considered unreliable and/or an artefact.

Considering the sequences in more detail, in the equiaxed mushy zone, the droplets streamed downwards from the top right of the FOV as indicated by the trajectory arrows. Qualitatively, the flow appeared to the eye to be uniform in the FOV with similar direction and velocity. Most of the droplets had already formed outside the FOV and were swept into it by the liquid flow (although it could not be excluded that some droplets continued to form). As the α-Al grew, the average droplet velocity increased sharply in the first $10\,\mathrm{s}$ to reach approximately $80\,\mu\mathrm{m\,s^{-1}}$ (Fig. 7a). The corresponding liquid velocity, calculated from Eq. 6, ranged between $45\,\mu\mathrm{m\,s^{-1}}$ to $200\,\mu\mathrm{m\,s^{-1}}$ (Fig. 7b). At $t = 12s$ the Pb droplets began to decelerate as their size increased, although the liquid velocity remained approximately constant until $t = 17s$, after which it steadily decreased to $\sim 60\,\mu\mathrm{m\,s^{-1}}$ when $t = 40s$. At this point the solid fraction was > 0.7 and several hot tears formed due to insufficient feeding, as highlighted by the rectangles in Fig. 5i. For clarity Fig. 6 shows a zoomed in sequence of the formation of a hot tear in detail, with the final hot tearing spanning many grains.

In the case of the columnar mushy zone, the droplets mostly formed within the FOV and the flow was more spatially concentrated into two comparatively large channels ($60\,\mu\mathrm{m}$ to $120\,\mu\mathrm{m}$ width) between primary dendrite arms. As in the previous case the droplet velocity increased rapidly, in this case "dragged" upwards by the intense shrinkage-induced flow, stabilising at $\sim 70\,\mu\mathrm{m\,s^{-1}}$ after $t = 5s$ and then quickly dropping at $t = 11s$ just before the formation of hot tears (Fig. 7c). The flow localization is clearer in video2, which also shows that the Pb droplet velocities in the large channel

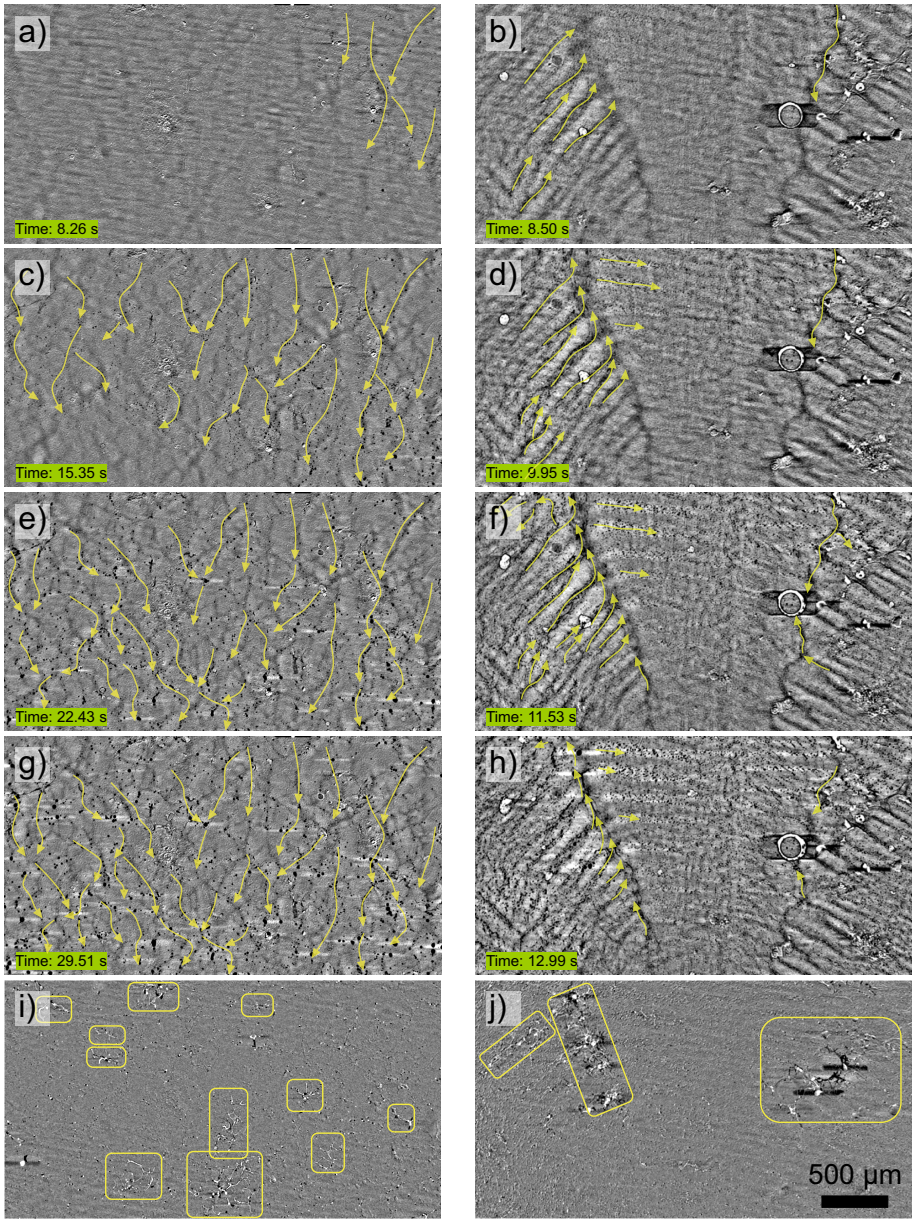

Figure 5: X-ray radiographic image sequences showing the movement of the Pb droplets within inter-dendritic channels of a solidifying Al-1wt%Pb alloy. (a, c, e and g) Al-1wt%Pb grain refined with TiB_2 and cooled near-isothermally at $0.7\,\mathrm{K\,s^{-1}}$ with an equiaxed microstructure. (b, d, f and h) Al-1wt%Pb cooled near-isothermally at $2\,\mathrm{K\,s^{-1}}$ with a columnar microstructure. (i and j) are frames at the end of solidification enhanced to highlight the hot tears (each image was obtained by subtracting frame f_{n-15} from frame f_n). The arrow streamlines are guides to the principal direction of the Pb droplet movement.

on the left of the middle dendrite exceeded the temporal resolution of the detector for several seconds, corresponding to velocities $>2000\,\mu\mathrm{m\,s^{-1}}$. Similarly, the Al-rich liquid moved at a constant velocity of $95\,\mu\mathrm{m\,s^{-1}}$ for $\sim 7.5\,\mathrm{s}$ and then peaked at $\sim 180\,\mu\mathrm{m\,s^{-1}}$, corresponding to the increased velocity in the large channel seen in video2, before hot

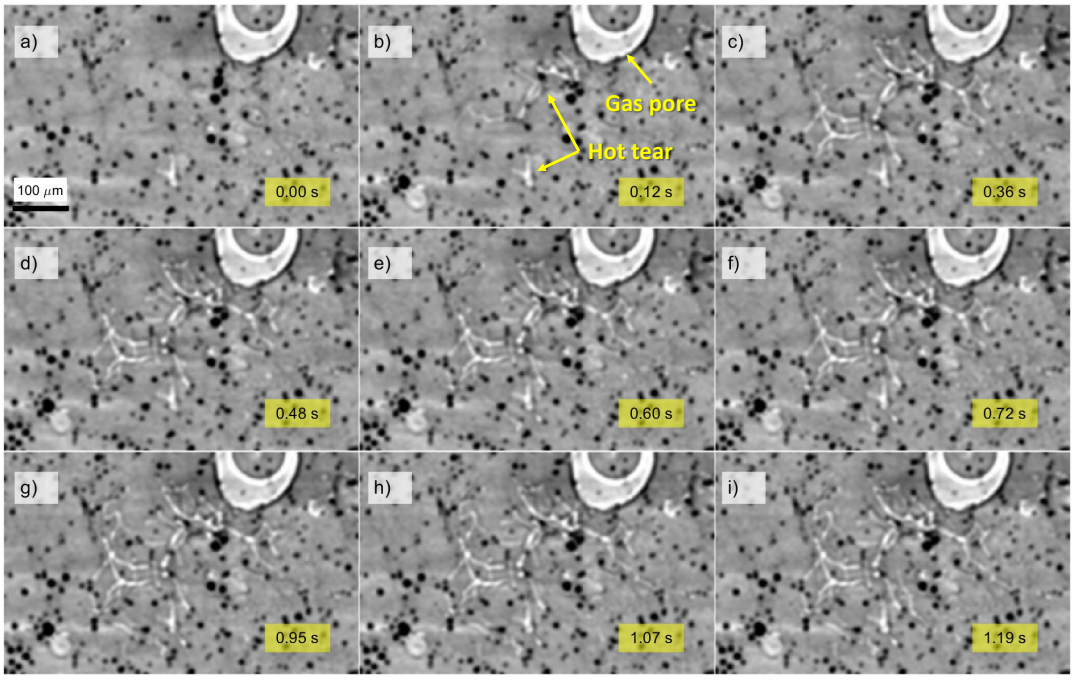

Figure 6: Image sequence showing the formation of a complex shaped hot tear (white).

tears formed. The peak velocity was likely underestimated due to the temporal resolution of the optical arrangement.

Fig. 8 shows the overall distribution, in a violin plot [42], of the average Al-rich liquid velocity at each time step for all five solidification sequences. Overall the equiaxed alloys showed consistently higher velocities. There was no correlation of velocity with cooling rate. The velocity distributions were asymmetric with long tails towards high velocities. Within the equiaxed mushy zone, the flow had a median velocity between $114\,\mu\mathrm{m\,s^{-1}}$ and $152\,\mu\mathrm{m\,s^{-1}}$ and 50% of the velocities were between $62\,\mu\mathrm{m\,s^{-1}}$ and $231\,\mu\mathrm{m\,s^{-1}}$, with a maximum of $420\,\mu\mathrm{m\,s^{-1}}$. For the columnar microstructure, the median velocities were between $86\,\mu\mathrm{m\,s^{-1}}$ and $140\,\mu\mathrm{m\,s^{-1}}$, while second and third quartiles were at $47\,\mu\mathrm{m\,s^{-1}}$ to $213\,\mu\mathrm{m\,s^{-1}}$, and the maximum velocity was $410\,\mu\mathrm{m\,s^{-1}}$.

The mushy zone pressure drop calculated using Eq. 7 is shown in Fig. 9, again as a violin plot. As for the liquid velocity, the pressure drop distributions were asymmetric. Higher cooling rates corresponded to narrower distributions for the columnar microstructures, but there was the opposite trend for equiaxed microstructures. Overall, pressure drops ranged between $-0.2\,\mathrm{kPa}$ to $-164\,\mathrm{kPa}$ (although outlier pressure drops were as low as $-440\,\mathrm{kPa}$). For equiaxed microstructures, the median pressure decreased from

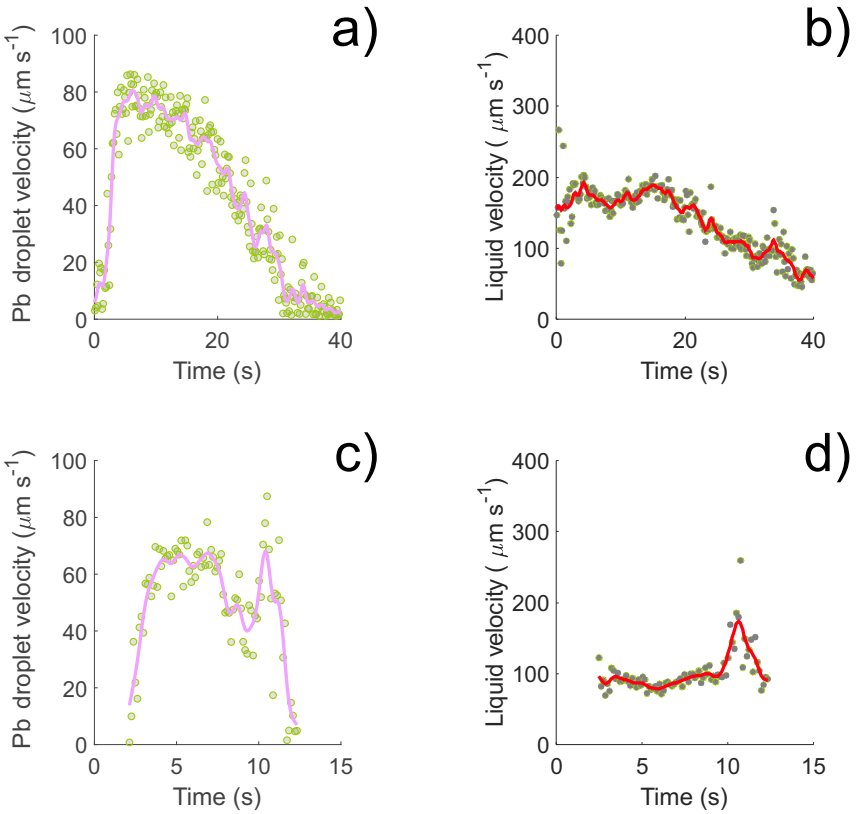

Figure 7: Pb droplets and Al-rich liquid average velocities for the two image sequences shown in Fig. 5. (a,b) equiaxed and (c,d) columnar microstructures.

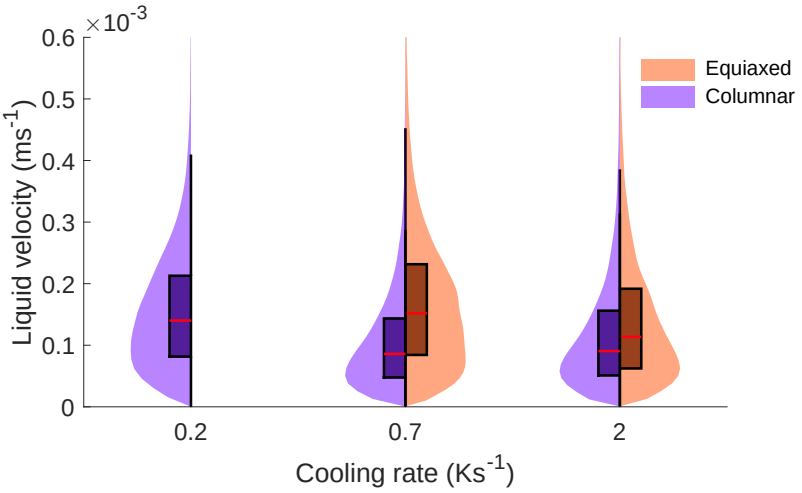

Figure 8: Distribution of the liquid velocity within the interdendritic channels visualized as violin plots. The box plot includes the second and third quartiles, the median velocity is indicated by the red line.

$-17\,\mathrm{kPa}$ at $0.7\,\mathrm{K\,s^{-1}}$ to $-50\,\mathrm{kPa}$ at $2\,\mathrm{K\,s^{-1}}$ and the minimum pressure from $-54\,\mathrm{kPa}$ to $-164\,\mathrm{kPa}$; for columnar microstructures, the median pressures were $-44\,\mathrm{kPa}$, $-12\,\mathrm{kPa}$ and $-8\,\mathrm{kPa}$ at $0.2\,\mathrm{K\,s^{-1}}$, $0.7\,\mathrm{K\,s^{-1}}$ and $2\,\mathrm{K\,s^{-1}}$ with corresponding minima of $-148\,\mathrm{kPa}$, $-43\,\mathrm{kPa}$ and $-24\,\mathrm{kPa}$.

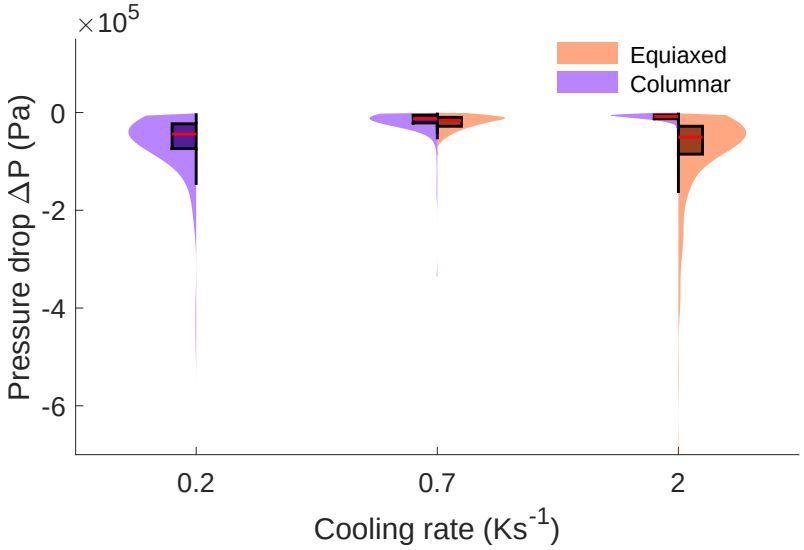

Figure 9: Distribution of the pressure drop within the mushy zone visualized as violin plots. The box plot includes the second and third quartiles, the median pressure is indicated by the red line.

By analysing the trajectories of the Pb droplets from each video sequence, the average width of the interdendritic channels could be estimated. Maps of the channel width for the two solidification sequences in Fig. 5 are shown in Fig. 10. The channel morphology in the equiaxed mushy zone (Fig. 10a) was more ramified with higher apparent tortuosity compared with columnar microstructures (Fig. 10b). Furthermore, although the average channel width was similar at $\sim 20\,\mu\mathrm{m}$, the channel widths in equiaxed microstructure were more uniform whereas the columnar mushy zone had a few noticeably wider channels at grain boundaries (Fig. 10b).

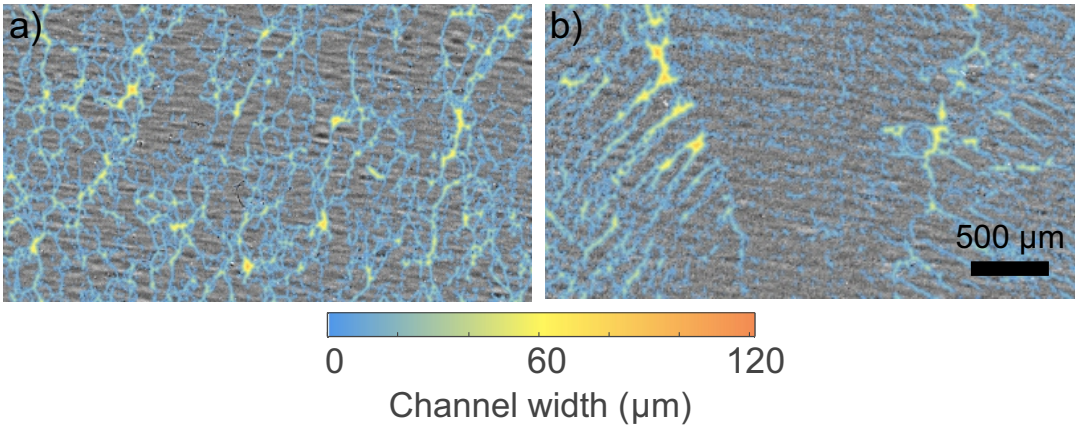

Figure 10: Average width of the interdendritic channels for the (a) equiaxed and (b) columnar sequences shown in Fig. 5 obtained by analysing the flow traces of the Pb droplets within each sequence.

5 Discussion

The video sequences revealed that solidification shrinkage led to long-range, complex flow patterns within the intricate morphology of the interdendritic channels. The liquid velocity evolved, dramatically in some cases, as the solid fraction increased around the monotectic freezing point, reaching $>500\,\mu\mathrm{ms}^{-1}$ in both columnar and equiaxed microstructures. Liquid velocities of up to $500\,\mu\mathrm{ms}^{-1}$ were also reported by Agarwal *et al.* [20] in a laser scanning confocal microscopy study on liquid feeding during the solidification of a dual phase steel, cooled at a cooling rate of $0.08\,\mathrm{K\,s}^{-1}$. Using a 3-D granular model, Sistaninia *et al.* [15] simulated liquid flow within the mushy zone of a Al-1Cu (wt%) DC cast round billet with globular microstructure. They reported simulated velocities of up to $150\,\mu\mathrm{ms}^{-1}$, in good agreement with the median values of $114\,\mu\mathrm{ms}^{-1}$ and $152\,\mu\mathrm{ms}^{-1}$ measured in the current work for an equiaxed microstructure.

The overall velocity distribution did not vary significantly between experiments, as shown in Fig. 8; however, the uniformity of the flow within each sequence was notably different for the equiaxed and columnar microstructures. This difference was related to the distribution of the size, shape and interconnectivity of the interdendritic channels, which in turn depended on the morphology of the pre-formed α-Al grains. When equiaxed, channels were tortuous and randomly orientated with a relatively uniform width of $10\,\mu\mathrm{m}$ to $25\,\mu\mathrm{m}$ within the FOV. When columnar, larger channels up to $60\,\mu\mathrm{m}$ of width formed at grain boundaries, along with relatively straight, preferentially oriented narrower channels between secondary dendrite arms.

The effect of the mushy zone morphology on the flow is more evident in Fig. 11, which compares the spatial variation of the maximum velocities measured in the two sequences in Fig. 5, obtained by binning the FOV into an array of sub-areas, each of area $330 \times 330\,\mu\mathrm{m}^2$. Each point is the ratio between the maximum velocity recorded within the spatial bin and the lowest maximum velocity within the entire FOV, effectively mapping the flow uniformity. The flow in the equiaxed microstructure was relatively uniform as indicated by the comparatively flat distribution of the normalised maximum velocity. On the contrary, in the columnar microstructure, there was strong localization of the flow at certain points, with local maximum velocities increased by as much as

twenty-fold. This velocity localization was not only spatial, but also temporal as shown by the peak in average instantaneous velocity in Fig. 7d. This trend was observed in all experiments, and a comparison of the standard deviation of the maximum velocities (as a measure of variability) suggested that the distribution of velocities increased with cooling rate: from 0.71 to 1.04 when cooling at $0.7\,\mathrm{K\,s^{-1}}$ and $2\,\mathrm{K\,s^{-1}}$ for equiaxed grains, and from 1.19 to 1.98 and 5.5 when cooled at $0.2\,\mathrm{K\,s^{-1}}$, $0.7\,\mathrm{K\,s^{-1}}$ and $2\,\mathrm{K\,s^{-1}}$ for columnar grains. It is tempting to speculate on the underlying reasons for this and possible other apparent correlations. However, given the variability of microstructure even in a single FOV, we recommend that larger datasets and strengthened confidence in estimates of, for example, solid fraction and permeability, are needed to draw additional robust insights.

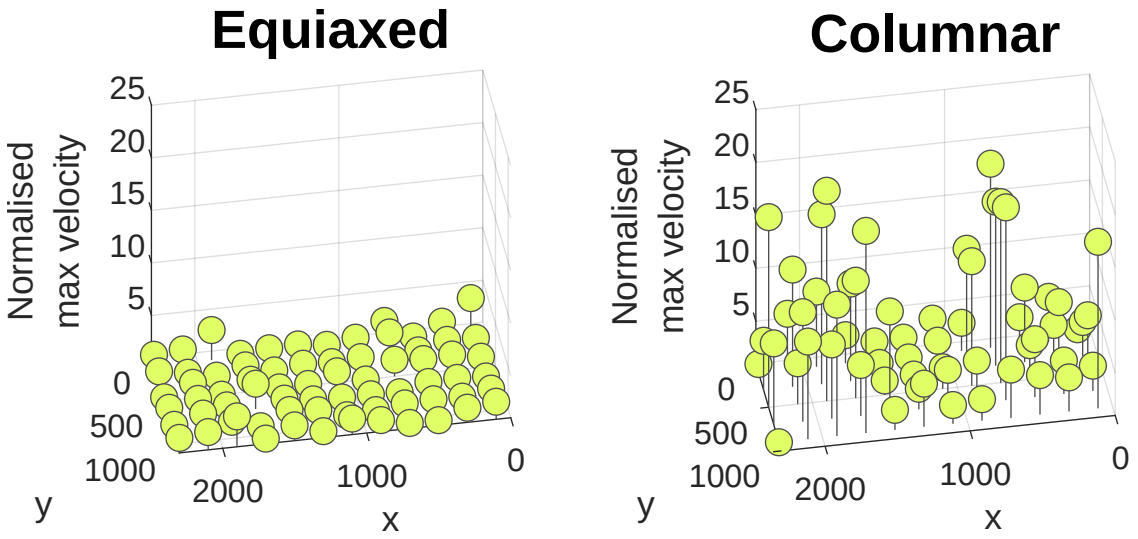

Figure 11: Normalized maximum velocity distribution for the sequences in Fig. 5. Each data point was obtained by dividing the FOV into bins of area $330 \times 330\,\mu\mathrm{m}$ and recording the maximum velocity in each bin over the entire solidification sequence. Maximum velocities of each bin area were then normalised by dividing them by the lowest maximum velocity in the FOV.

The evolution of the pressure drop within the mushy zone (Fig. 9) varied between -0.3 kPa and -415 kPa, and these data lie within the range measured for a dual-phase steel [20], predicted using a 3-D granular model simulation for Al-Cu alloys [15–17], and predicted for an AA5182 DC cast billet [18]. However the current approach suggests that even for a single region of microstructure, the pressure drops are highly disperse and sensitive to the details of the local structure such as interdendritic channel width. It can be conjectured that specific regions experiencing the most dramatic pressure drops are those most likely to initiate a hot tear, and this is focus of our current work based

on analysis of a much larger dataset.

Fig. 12 plots the calculated median pressure drop over the entire FOV measured at each time step as a function of the equivalent solid fraction f_s. The pressure decreased monotonically with increasing solid fraction, with slightly different shape for equiaxed and columnar microstructures due to different permeabilities for a given solid fraction. The continuous lines are the best-fit to the data, using a general exponential function, and the yellow symbols indicate the appearance of the first hot tear in the FOV during experiment, i.e. the critical pressure drop for hot tear formation. The critical pressure drop lay between $-21\,\mathrm{kPa}$ and $-73\,\mathrm{kPa}$ for equiaxed microstructures and between $-8\,\mathrm{kPa}$ and $-47\,\mathrm{kPa}$ for columnar microstructures, and at a solid fraction between 0.76 and 0.88. These critical solid fractions for hot tear formation are consistent with the literature: between 0.78 and 0.9 for a Mg-Al-Sr alloy [43]; between 0.88 and 0.98 in a M206 aluminium casting alloy [44]; and between 0.93 and 0.96 for a Al-0.5Cu alloy [45]. However, they are slightly lower than the critical solid fraction predicted for an Al-1Cu alloy using a strain rate sensitive model [15], a factor not easily interpreted from the current experiments. A further source of discrepancy may arise from the 2D geometry of samples used in our experiment, which might be more susceptible to tearing compared with the greater extent of geometric interlocking that can be expected in the 3D structure of a large casting.

The critical pressure drop ΔP_c for hot tearing has been proposed to relate to the width of interdendritic channels as [16]:

$$\Delta P_c = \frac{\lambda cos\Theta}{h} \tag{10}$$

where λ is the surface tension at the void–liquid interface and Θ is the dihedral angle. Fig. 13 plots ΔP_c from Fig. 12 as a function of the halfwidth h of the largest interdendritic channel within the region where the first hot tear formed measured from the radiographs. Fig. 13 also shows a best-fit of Eq. 10 to the data assuming $\lambda cos\Theta = 2$ [16], with a reasonable fit to the data. However, the data covers only a limited range of channel sizes and more measurements (i.e. a greater range of microstructures) are needed to assert the validity of Eq. 10 more robustly, or to propose alternatives.

The methodology has considerable scope for improvement, such as using higher

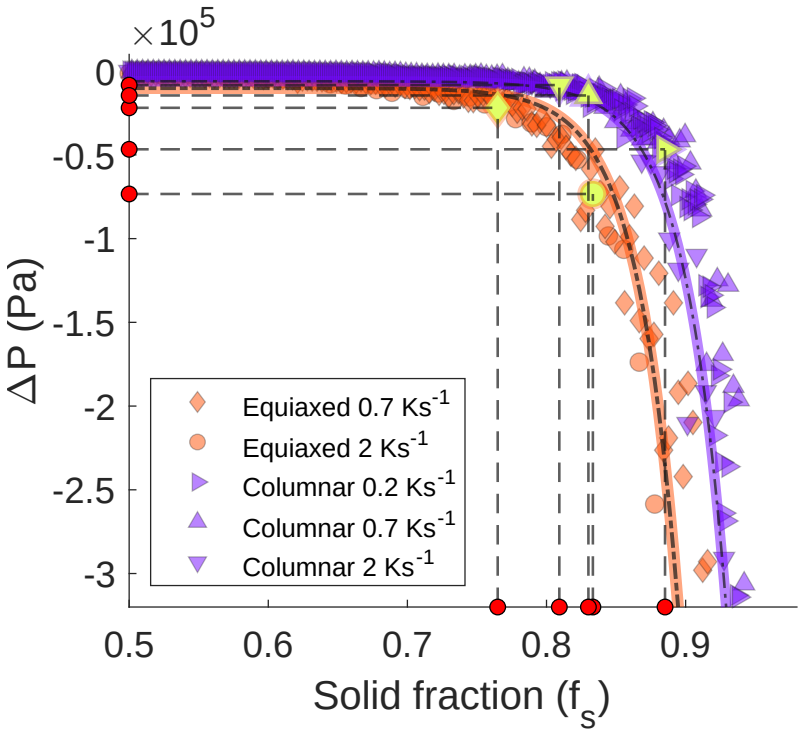

Figure 12: Median pressure drop evolution in the FOV as a function of solid fraction for all the experiments and grouped by microstructure. The yellow markers are the ΔP_c and f_{sc} values at which the first hot tear appeared in the radiograph; the critical pressure drop and solid fraction are indicated by the red circles on the x-y axes.

spatio-temporal resolution imaging conditions to increase the precision of the droplet tracking, and more accurate experimental estimation of the evolution of permeability and solid fraction would be particularly useful. Droplet tracking has been demonstrated for a simple binary monotectic Al-Pb alloy that concentrated the shrinkage and the induced Pb droplet and liquid flow into a narrow temperature range during which the α-Al solid fraction evolved quickly. Future work might consider other alloy systems where solid fraction evolution is more gradual with temperature and time and the detailed tracking of the tracer droplets perhaps made easier. However, under these conditions the simplifying assumptions required for convenient analysis of images, for example relating to the Marangoni forces acting on droplets, may become more problematical. Since the use of thin ($\sim$200 µm) foils required for radiography precludes a realistic 3-D mushy zone and related flow, the approach might be extended to time-resolved tomography, if a sufficiently fast acquisition rate could be achieved. However, the subsequent 3D data processing required to obtain the critical parameters would represent a major challenge.

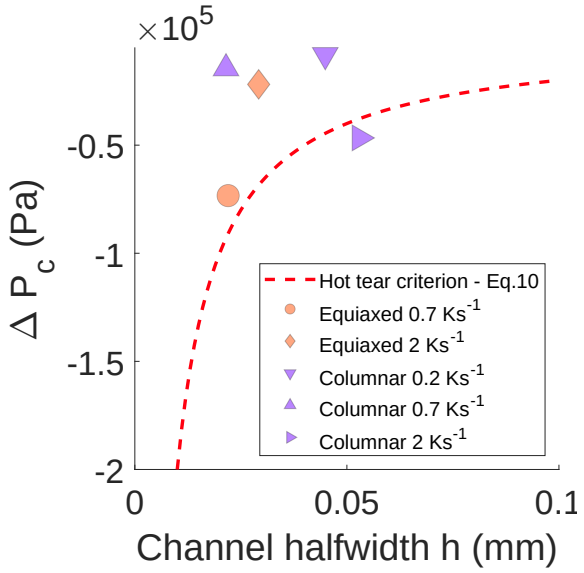

Figure 13: Experimental and analytical plots of critical pressure for hot tearing as a function of channel size. The dashed line is a best-fit to Eq. 10 representing a proposed relationship between interdendritic channel width and critical pressure drop for hot tear formation. The experimental data points were obtained using the pressure drop within the entire FOV in the frame before the appearance of the first hot tear and the size of the largest channel measured in the region where the hot tear formed.

6 Conclusions

A novel experimental methodology based on X-ray radiography and image analysis has been developed to track micron-sized, dense tracer droplets (thousands in each video sequence) during the shrinkage-induced interdendritic flow of a solidifying Al-Pb alloy. Analysis has been developed that uses the spatially and temporally resolved droplet flow data to quantify the evolution of the velocity of the interdendritic liquid during the final stages of solidification. A series of assumptions were required to achieve a tractable analysis, and the validity and limits of these assumptions have been discussed. Liquid velocities were then related to the associated pressure drop experienced by the liquid due to liquid to solid shrinkage, as a function of the shape, size and connectivity of the inter-dendritic channel network, for both equiaxed and columnar microstructures. Measured liquid velocities and the associated pressure drops were consistent with previous, mainly simulation-led, reports, although the spatial distribution and microstructural effects on pressure drop are reported here for the first time. Average pressure drops were correlated with the formation of hot tears that could also be resolved in the radiographic sequences, and showed trends that help to validate assumptions made in prior work. With relatively

straightforward improvements in spatial and temporal resolution, the approach may offer significant potential to probe the final stages of alloy solidification in detail, including revealing the dynamics of the critical hot tearing phenomenon.

7 Acknowledgements

This work was supported by EPSRC (UK) under grant number EP/H026177/1 (LiME) and EP/N007638/1 (Future Liquid Metal Engineering Hub). The synchrotron work was enabled by beamtime MT9140 at the Diamond Light Source B16 beamline. The authors would also like to thank Martin Jarret and Paula Camean Queijo for their help in the preparation of the samples.

References

1. Campbell, J. *Complete Casting Handbook* 1st. ISBN: 1856178099 (Butterworth-Heinemann, 2011).
2. Dantzig, J. & Rappaz, M. *Solidification* 2st. ISBN: 2940222975 (EPFL Press, 2017).
3. Rappaz, M. Modeling and characterization of grain structures and defects in solidification. *Current Opinion in Solid State and Materials Science* **20,** 37–45 (2016).
4. Cho, S. M. & Thomas, B. G. Electromagnetic Effects on Solidification Defect Formation in Continuous Steel Casting. *JOM* **72,** 3610–3627 (2020).
5. Song, J. *et al.* A review on hot tearing of magnesium alloys. *Journal of Magnesium and Alloys* **4,** 151–172 (Sept. 2016).
6. Nabawy, A. M., Samuel, A. M., Doty, H. W. & Samuel, F. H. A Review on the Criteria of Hot Tearing Susceptibility of Aluminum Cast Alloys. *International Journal of Metalcasting,* 1–13 (2021).
7. Li, Y. *et al.* Recent advances in hot tearing during casting of aluminium alloys. *Progress in Materials Science* **117,** 100741 (2021).
8. Lu, Y., Bartlett, L. N. & O'Malley, R. J. A Review on Hot Tearing of Steels. *International Journal of Metalcasting,* 1–17 (2021).

9. Li, S. & Apelian, D. Hot tearing of aluminum alloys a critical literature review. *International Journal of Metalcasting* **5,** 23–40 (2011).

10. Rappaz, M., Drezet, J. .-. & Gremaud, M. A new hot-tearing criterion. *Metallurgical and Materials Transactions A* **30,** 449–455. ISSN: 1073-5623 (1999).

11. Farup, I., Drezet, J. M. & Rappaz, M. In situ observation of hot tearing formation in succinonitrile-acetone. *Acta Materialia* **49,** 1261–1269 (Apr. 2001).

12. Vernède, S., Jarry, P. & Rappaz, M. A granular model of equiaxed mushy zones: Formation of a coherent solid and localization of feeding. *Acta Materialia* **54,** 4023–4034 (Sept. 2006).

13. Phillion, A. B., Vernède, S., Rappaz, M., Cockcroft, S. L. & Lee, P. D. Prediction of solidification behaviour via microstructure models based on granular structures. *International Journal of Cast Metals Research* **22,** 240–243 (2009).

14. Monroe, C. & Beckermann, C. Prediction of Hot Tearing Using a Dimensionless Niyama Criterion. *JOM* **66,** 1439–1445. ISSN: 1047-4838 (Aug. 2014).

15. Sistaninia, M., Phillion, A. B., Drezet, J. M. & Rappaz, M. Three-dimensional granular model of semi-solid metallic alloys undergoing solidification: Fluid flow and localization of feeding. *Acta Materialia* **60,** 3902–3911. ISSN: 13596454 (2012).

16. Sistaninia, M., Phillion, A. B., Drezet, J.-M. M. & Rappaz, M. A 3-D coupled hydromechanical granular model for simulating the constitutive behavior of metallic alloys during solidification. *Acta Materialia* **60,** 6793–6803. ISSN: 13596454 (Nov. 2012).

17. Sistaninia, M., Terzi, S., Phillion, A. B., Drezet, J.-M. & Rappaz, M. 3-D granular modeling and in situ X-ray tomographic imaging: A comparative study of hot tearing formation and semi-solid deformation in Al–Cu alloys. *Acta Materialia* **61,** 3831–3841. ISSN: 13596454 (June 2013).

18. Sistaninia, M., Drezet, J.-M., Phillion, A. B. & Rappaz, M. Prediction of Hot Tear Formation in Vertical DC Casting of Aluminum Billets Using a Granular Approach. *JOM* **65,** 1131–1137. ISSN: 1047-4838 (Sept. 2013).

19. Stefanescu, D. M. Computer simulation of shrinkage related defects in metal castings - A review. *International Journal of Cast Metals Research* **18,** 129–143 (2005).

20. Agarwal, G. *et al.* Experimental evidence of liquid feeding during solidification of a steel. *Scripta Materialia* **146,** 105–109. ISSN: 13596462. http://linkinghub.elsevier.com/retrieve/pii/S1359646217306346 (Mar. 2018).

21. Liotti, E. *et al.* A synchrotron X-ray radiography study of dendrite fragmentation induced by a pulsed electromagnetic field in an Al-15Cu alloy. *Acta Materialia* **70,** 228–239. ISSN: 13596454 (2014).

22. Liotti, E. *et al.* Crystal nucleation in metallic alloys using x-ray radiography and machine learning. *Science Advances* **4,** eaar4004. ISSN: 23752548 (Apr. 2018).

23. Feng, S., Liotti, E., Wilson, M. D., Jowitt, L. & Grant, P. S. In situ mapping of chemical segregation using synchrotron x-ray imaging. *MRS Bulletin* **45,** 934–942. ISSN: 0883-7694 (2020).

24. Yu, S.-K., Sommer, F. & Predel, B. 20180927173829097.pdf. *Zeitschrift für Metallkunde* **87,** 574–580 (1996).

25. Adrian, R. J. & Westerweel, J. *Particle Image Velocimetry* 1st (Cambridge University Press, 2011).

26. Farnebäck, G. Two-Frame Motion Estimation Based on Polynomial Expansion, 363–370 (2003).

27. Schaffer, P. L., Mathiesen, R. H., Arnberg, L., Di Sabatino, M. & Snigirev, A. In situ investigation of spinodal decomposition in hypermonotectic Al-Bi and Al-Bi-Zn alloys. *New Journal of Physics* **10.** ISSN: 13672630 (2008).

28. Schaffer, P. L., Mathiesen, R. H. & Arnberg, L. Liquid decomposition, droplet coagulation and droplet-interface interactions in hypermonotectic Al-Bi alloys. *Transactions of the Indian Institute of Metals* **62,** 437–442 (2009).

29. Schaffer, P. L., Mathiesen, R. H. & Arnberg, L. L-2 droplet interaction with alpha-Al during solidification of hypermonotectic Al-8 wt.% Bi alloys. *Acta Materialia* **57,** 2887–2895 (2009).

30. Zhao, J. Z., Ratke, L. & Feuerbacher, B. Microstructure evolution of immiscible alloys during cooling through the miscibility gap. *Modelling and Simulation in Materials Science and Engineering* **6,** 123–139 (Mar. 1998).

31. Kaban, I. *et al.* Interfacial tension, wetting and nucleation in Al–Bi and Al–Pb monotectic alloys. *Acta Materialia* **59,** 6880–6889 (2011).

32. Wu, M., Ludwig, A. & Ratke, L. Modeling of marangoni-induced droplet motion and melt convection during solidification of hypermonotectic alloys. *Metallurgical and Materials Transactions A* **34,** 3009–3019 (2003).

33. Ratke, L. & Thieringer, W. K. The influence of particle motion on ostwald ripening in liquids. *Acta Metallurgica* **33,** 1793–1802 (1985).

34. Ratke, L. & Diefenbach, S. Liquid immiscible alloys. *Materials Science and Engineering R* **15,** 263–347 (1995).

35. Zhao, J. Z. & Ratke, L. A model describing the microstructure evolution during a cooling of immiscible alloys in the miscibility gap. *Scripta Materialia* **50,** 543–546 (2004).

36. Zhao, J. Z., He, J., Hu, Z. Q. & Ratke, L. Microstructure evolution in immiscible alloys during rapid directional solidification. *Zeitschrift fuer Metallkunde/Materials Research and Advanced Techniques* **95,** 362–368 (2004).

37. Kirshenbaum, A. D., Cahill, J. A. & Grosse, A. V. The density of liquid lead from the melting. *Journal of Inorganic and Nuclear Chemistry* **22,** 33–38 (1961).

38. Iida, T. & Guthrie, R. *The thermophysical properties of liquid metals. Volume 1: Fundamentals* first. ISBN: 9780198729839 (Oxford University Press, 2015).

39. Poirier, D. R. Permeability for flow of interdendritic liquid in columnar-dendritic alloys. *Metallurgical Transactions B* **18,** 245–255 (1987).

40. Puncreobutr, C., Phillion, A. B., Fife, J. L. & Lee, P. D. Coupling in situ synchrotron X-ray tomographic microscopy and numerical simulation to quantify the influence of intermetallic formation on permeability in aluminium-silicon-copper alloys. *Acta Materialia* **64,** 316–325 (2014).

41. Duncan, A. J., Han, Q. & Viswanathan, S. Measurement of liquid permeability in the mushy zones of aluminum-copper alloys. *Metallurgical and Materials Transactions B: Process Metallurgy and Materials Processing Science* **30,** 745–750 (1999).

42. Hintze, J. L. & Nelson, R. D. Violin plots: A box plot-density trace synergism. *American Statistician* **52,** 181–184. ISSN: 15372731 (1998).

43. Cao, G., Haygood, I. & Kou, S. Onset of hot tearing in ternary Mg-Al-Sr alloy castings. *Metallurgical and Materials Transactions A: Physical Metallurgy and Materials Science* **41,** 2139–2150 (2010).

44. Li, S., Sadayappan, K. & Apelian, D. Characterisation of hot tearing in Al cast alloys: Methodology and procedures. *International Journal of Cast Metals Research* **24,** 88–95 (2011).

45. Davidson, C., Viano, D., Lu, L. & Stjohn, D. Observation of crack initiation during hot tearing. *International Journal of Cast Metals Research* **19,** 59–65 (2006).